DOI: 10.1021/ic9019958

Inorganic Chemistry
Article

Experimental Charge Density Analysis of Symmetrically Substituted Ferrocene Derivatives

Anna M. Makal,[†] Damian Plażuk,[‡] Janusz Zakrzewski,[‡] Bogusław Misterkiewicz,[§] and Krzysztof Woźniak*[,†]

[†]*Department of Chemistry, Warsaw University, Pasteura 1, 02-093 Warszawa, Poland,*
[‡]*Department of Organic Chemistry, University of Łódź, Narutowicza 68, 90-136 Łódź, Poland, and*
[§]*Instytut of Organic Chemistry, The Technical University of Radom, Chrobrego 27, 26-600 Radom, Poland*

Received October 12, 2009

Experimental charge density analysis of three symmetrically substituted ferrocene derivatives: 1,1′- dimethyl ferrocene (**1**), decamethyl ferrocene (**2**), and 1,1′-diacetyl ferrocene (**3**) was conducted. The electron donating or accepting propensities of the ferrocene substituents were evaluated. The metal ligand interactions in all analyzed compounds were found to be similar in terms of charge density concentrations at Bond Critical Points (BCPs), laplacian values, and deformation density features. The monopole population of iron in all cases tend to be slightly negative, suggesting charge donation from Cp ligands. d orbital populations in all cases adopt values in agreement with theoretical calculations and ligand field theory. The charge distribution over analyzed molecules does not correlate with the formal oxidation potential in the analyzed compounds, as compound **2** in the currently studied structure takes the place suitable for an unsubstituted ferrocene. The non-intuitive low energy of the eclipsed conformation of **1** compound finds some explanation in the existence of a bond critical point between atoms of the two methyl groups in the structure. An asymmetry of the atomic surroundings of the two oxygen atoms in the **3** structure, reflected by the differences in charge $\rho(r_{BCP})$ and $\nabla^2\rho(r_{BCP})$ values and the shape of deformation density in the regions of oxygen lone electron pairs, is described.

Introduction

Since its discovery in 1951, ferrocene has played an important role in organometallic chemistry. Because of its stability and the ability to easily undergo an iron oxidation reaction, its derivatives found applications in many fields, especially in electrochemistry and, more recently, biochemistry and drug design. In bioelectrochemistry, ferrocene and its derivatives are applied as mediators of protein redox reactions[1] and as internal standards[2,3]. Ferrocene used to be considered as a IUPAC standard for electrochemical processes in aqueous solutions[4]. A few ferrocene derivatives have been lately discovered to possess potential anticancer propensities, and in particular to form a useful analogue to tamoxifen[5]. Ferrocene derivatives are very good examples of an aromatic compound sensitive to the influence of electron-withdrawing (EWG) and electron-donating (EDG) substituents. The electron donating/withdrawing effects of a number of moieties have been established by the measurements of the influence of those moieties on the oxidation potentials of the ferrocene substituted by such a moiety[6]. A relation between the ferrocene derivative oxidation potential and a Hammett σ_p constant of the ferrocene substituent has been reported[7]. The formal oxidation potentials of selected ferrocene derivatives, ordered according to the diminishing EWG properties of the ferrocene substituents, are presented in Table 1.

The strict influence of the structural modifications on the electrochemical behavior of ferrocene, as well as unique geometry of the metal−ligand connection in ferrocene-like sandwich complexes make them interesting objects for charge density studies. As the iron in a sandwich complex is sensitive to the electron-withdrawing strength of cyclopentadienyl (Cp) ring substituents, its bonding with the Cp ligands must be strong and worth a detailed description. Several ferrocene-derivative studies by means of quantum mechanical

*To whom correspondence should be addressed. E-mail: kwozniak@chem.uw.edu.pl. Phone: +48 22 8220211, ext. 212. Fax: +48 22 8220211, ext. 212.

(1) (a) *Bioorganometallics: biomolecules, labeling, medicine*; Jaouen, G., Ed.; Wiley-VCH: Weinheim, 2006; (b) Dai, Z. H.; Ni, J.; Huang, X. H.; Lu, G. F.; Bao, J. C. *Bioelectrochemistry* **2007**, *70*(2), 250–256. (c) *Ferrocenes: Ligands, Materials and Biomolecules*, Ed.Stepnicka, P., Ed.; John Wiley&Sons, Ltd: New York, 2008. (d) *Ferrocenes: homogeneous catalysis, organic synthesis, materials science*; Ed. by Togni, A., Hayashi, T., Eds.; VCH: Weinheim, 1995.

(2) Carney, M. J.; Lesniak, J. S.; Likar, M. D.; Pladziewicz, J. R. *J. Am. Chem. Soc.* **1984**, *106*, 2565–2569.

(3) Degani, Y.; Heller, A. *J. Am. Chem. Soc.* **1980**, *110*, 2615–2620.

(4) Gritzner, G.; Kuta, J. *Pure Appl. Chem.* **1984**, *56*(4), 461–466.

(5) Top, S.; Vessières, A.; Leclercq, G.; Quivy, J.; Tang, J.; Vaissermann, J.; Huché, M.; Jaouen, G. *Chem.—Eur. J.* **2003**, *9*, 5223–5236.

(6) Frantz, R.; Duranda, J. O.; Lanneau, G. J. *J. Organomet. Chem.* **2004**, *689*(11), 1867–1871.

(7) Nagy, A.; Toma, S. *J. Organomet. Chem.* **1985**, *282*, 267.

(8) Clegg, A. D.; Rees, N. V.; Klymenko, O. V.; Coles, B. A.; Compton, R. G. *J. Electroanal. Chem.* **2005**, *580*, 78–86.

Published on Web 04/06/2010

Scheme 1. Representations of the Analyzed Compounds (a) **1**, (b) **2**, and (c) **3**

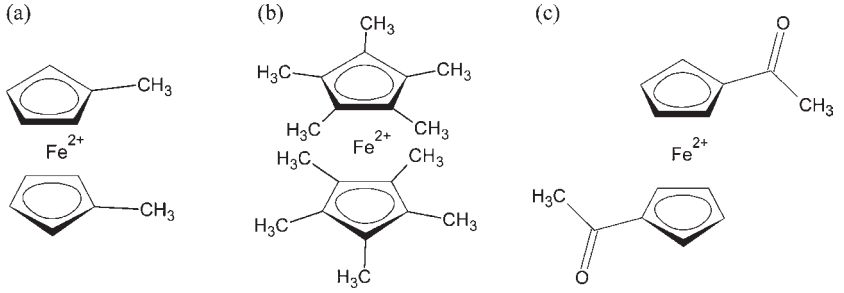

Table 1. Formal $Fe^{2+/3+}$ Oxidation Potentials for a Series of Differently Substituted Ferrocene Derivatives As Obtained in Acetonitrile at High Speed Channel Electrode[8] (HSChE)[a]

compound	E_f [V]
ferrocene carboxylic acid	0.794(2)
ferrocene carboxyaldehyde	0.786(15)
dimethyl aminoethyl ferrocene	0.584(3)
α-hydroxyethyl ferrocene	0.394(3)
ferrocene	0.371(7)
dimethyl ferrocene (compound **1**)	*0.367(5)*
tert-buthyl ferrocene	0.310(9)
decamethyl ferrocene (compound **2**)	*0.113(1)*

[a] The compounds included in present study are presented in italics.

calculations, using a range of basis sets and methods, have been conducted so far[9]. However, only a few experimental charge density studies have been undertaken. The first purely qualitative description of the charge density distribution around the metallic center in a series of η5-sandwich complexes of first row transitional metals was reported in 2001[10]. In 2008 the (*E*)-1,2-fluoro-1,2-ferrocenyl ethene ferrocene derivative was described in terms of experimental charge density analysis and theoretical calculations by Farrugia et al.[11] The authors concentrated on the applicability of the Bader's theory of Atoms in Molecules (AIM)[12] in the description of metal−ligand interaction in sandwich and half-sandwich metal complexes.

Ferrocene itself present difficulties in obtaining experimental X-ray data appropriate for charge density analysis. There are three polymorphic crystal structures of ferrocene reported to date, one of them being an example of severe dynamic disorder in one of the η5-ligands[13]. The remaining two[14,15] polymorphs are only stable at very low temperatures, and obtaining well diffracting crystals in their case is challenging.

In this study, we present the results of experimental charge density analysis for a series of three symmetrically substituted ferrocene derivatives, namely, 1,1′- dimethyl ferrocene, decamethyl ferrocene, and 1,1′- diacetyl ferrocene (Scheme 1, Figure 1). The compounds are well-known for their applicability in electrochemistry[16,17], and in synthesis of more complicated derivatives[18]. The first two, further denoted as **1** and **2** accordingly, represent a ferrocene modified by addition of different number of simple EDG substituents. Their formal oxidation potentials, both lower than that obtained for ferrocene, are already listed in Table 1, illustrating the tendency of the formal oxidation potential to get less positive as the number or strength of the EDG substituents increases. The third (**3**), containing two strong EWG substituents is expected to display a formal potential similar or higher than ferrocene carboxyaldehyde.

One of the aims of the current work is the evaluation of the character of the ferrocene substituents in terms of the topological properties of experimental charge density and charges concentrated on atoms and molecular fragments. Another aim is the description of metal−ligand interactions in the series of presented compounds from the experimental charge density point of view. Finally, although molecules of all three compounds may be expected to adopt highly symmetrical conformations, the molecules **1** and **3** present some distortions from ideal symmetry, apparently because of the intermolecular interactions in the crystal lattice. Therefore, we would like to check whether those intermolecular interactions manifest themselves in terms of topological features of charge density in crystal such as Bond Critical Points (BCPs) and bond paths.

The structure of **1** has been already determined at room temperature[19] and at 173 K[20]. The structure of **2** has been determined at room temperature[21,22], and at 150 K[23]. The structure of **3** has been determined at room temperature[24]. To obtain high quality and high-resolution data for all compounds, structures **2** and **3** were remeasured in the current study at 90 K, and structure **1** at 100 K.

Experimental Section

The data for **1**, **2**, and **3** were collected using the BRUKER KAPPA APEXII ULTRA controlled by APEXII software[25]

(9) Zhang, G.; Zhang, H.; Sun, M.; Liu, Y.; Pang, X.; Yu, X.; Liu, B.; Li, Z. *J. Comput. Chem.* **2007**, *28*, 2260–2274.
(10) Lyssenko, K. A.; Yu. Antipin, M.; Yu. Ketkov, S. *Russ. Chem. Bull. Int. Ed.* **2001**, *50*, 130–141.
(11) Farrugia, L. J.; Evans, C.; Lentz, D.; Roemer, M. *J. Am. Chem. Soc.* **2009**, *131*(3), 1251–1268.
(12) (a) Bader, R. F. W. *Atoms in Molecules: A Quantum Theory*; Oxford University Press: New York, 1990; (b) Bader, R. F. W. *J. Phys. Chem.* **1998**, *A102*, 7314–7323.
(13) Seiler, P.; Dunitz, J. D. *Acta Crystallogr.* **1979**, *B35*, 1068–1074.
(14) Seiler, P.; Dunitz, J. D. *Acta Crystallogr.* **1979**, *B35*, 2020–2032.
(15) Seiler, P.; Dunitz, J. D. *Acta Crystallogr.* **1982**, *B38*, 1741–1745.
(16) Su, B.; Nia, R. P.; Li, F.; Hojeij, M.; Prudent, M.; Corminboeuf, C.; Samec, Z.; Girault, H. H. *Angew. Chem., Int. Ed.* **2008**, *47*, 4675–4678.
(17) Morad, M. S.; Sarhan, A. A. O. *Corros. Sci.* **2008**, *50*, 744–753.
(18) Tebben, L.; Kehr, G.; Frohlich, R.; Erker, G. J. I. *Synthesis* **2004**, *12*, 1971–1976.
(19) Lousada, C. M.; Pinto, S. S.; Canongia Lopes, J. N.; Minas da Piedade, F. M.; Diogo, H. P.; Minas da Piedade, M. E. *J. Phys. Chem.* **2008**, *A112*, 2977–2987.
(20) Foucher, D. A.; Honeyman, C. H.; Lough, A. J.; Manners, I.; Nelson, J. M. *Acta Crystallogr.* **1995**, *C51*, 1795–1799.
(21) Struckhov, Y. T.; Andrianov, v. G.; Salnikova, T. N.; Laytifov, I. R.; Maternikova, R. B. *J. Organomet. Chem.* **1978**, *145*, 213–223.
(22) Freyberg, D. P.; Robbins, J. L.; Raymond, K. N.; Smart, J. C. *J. Am. Chem. Soc.* **1979**, *101*, 892.
(23) Arrais, A.; Diana, E.; Gobetto, R.; Milanesio, M.; Viterbo, D.; Stanghellini, P. L. *Eur. J. Inorg. Chem.* **2003**, 1186–1192.
(24) Palenik, G. J. *Inorg. Chem.* **1970**, *9*(11), 2424–2430.

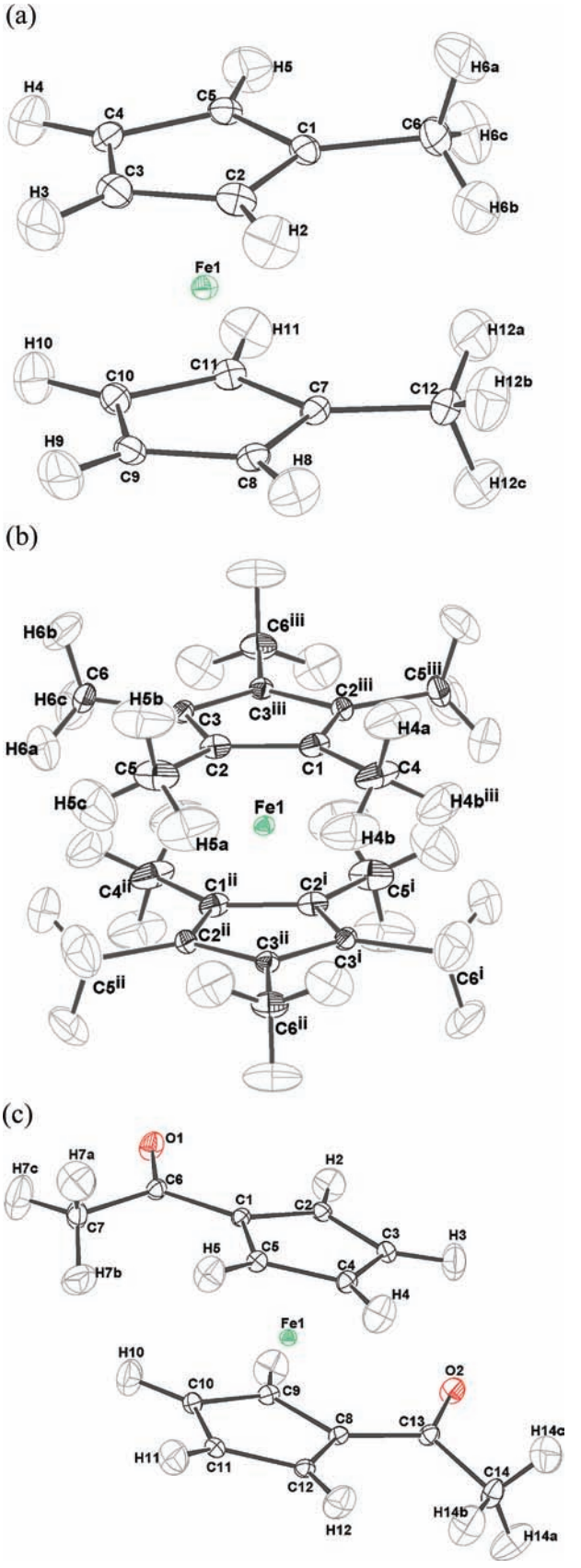

Figure 1. ORTEP representations of (a) **1**, (b) **2**, and (c) **3**. Ellipsoids drawn at 50% probability level. Hydrogen labels in **2** are reported for independent part of the molecule only. The symmetry operations in the structure **2** are denoted as follows: (i) $-x$, y, z; (ii) $-x$, $-y$, $-z$; (iii) x, $-y$, $-z$.

system and equipped with Mo Kα rotating anode X-ray source and APEX-II CCD detector. In the case of the **1** data set, the beam was monochromatized by a graphite monochromator, in other cases the beam was monochromatized and collimated by a set of multilayer focusing optics. The experiments were carried out using the Oxford Cryostream cooling device. Crystals were mounted on thin cactus needles with a droplet of Paratone-N oil and immediately cooled.

For **1**, a total of 3096 frames of 0.5° oscillation width, divided into 16 ω scans, were collected. The generator settings were 50 kV and 100 mA, and the crystal to detector distance was set to 40 mm. The exposure time per frame varied with the detector position in 2θ angle as follows: 5 s for 5° and 17.5°, 10 s for −37°, 15 s for −40° and +40°, 30 s for −45° and 47.5°, 60 s for 67° and 80 s for over 70°.

For **2**, a total of 2188 frames of 0.5° oscillation width in 13 ω scans were collected. The generator settings were 45 kV and 45 mA, and the crystal to detector distance was set to 40 mm. The exposure time per frame varied with the detector position in 2θ angle as follows: 4 s for 15° and −22.5°, 20 s for −30°, −47.5° and −50°, and 40 s for over 60°.

For **3**, a total of 2316 frames of 0.5° oscillation width in 15 omega scans were collected. The generator settings were 45 kV and 40 mA, and the crystal to detector distance was set to 40 mm. The exposure time per frame varied with the detector position in 2θ angle as follows: 6 s for 22.5°, 10 s for −30°, 15 s for −35° and +40°, 30 s for 47.5°, 50 s for 70°, 72,5°, 75° and 77.5° and 60 s for over 80°.

Indexing, integration, and initial scaling were performed with SAINT and SADABS software[26]. The unit cell parameters were obtained and refined based on the whole data sets. The absorption correction from crystal faces was applied before scaling for each sample. The average mosaicity was refined to the value of 0.6° in the case of **1** and **3** and 1.0° in the case of **2**. No decay of the samples during the measurements was observed. Finally the data sets were merged with SORTAV[27]. The data collection and processing statistics are given in Table 2.

Graphical representations of charge density topological features were prepared by a preliminary version of jdVis visualization software[28].

Structure Solution and Conventional Refinement. The structures were solved by the direct methods approach using the SHELXS-97 program[29] and then refinements based on F^2 except reflections with negative intensities were carried out with the SHELXL-97[30]. Weighted R factors wR and all goodness-of-fit S values were based on F^2, whereas conventional R factors were based on the amplitudes, with F set to zero for negative F^2. The $F_0^2 > 2\sigma(F_0^2)$ criterion was applied only for R factors calculation and was not relevant to the choice of reflections for the refinement. The R factors based on F^2 are for all structures about twice as large as those based on F. Scattering factors were taken from Tables 4.2.6.8 and 6.1.1.4 from the International Crystallographic Tables Vol. C[31]. In the final refinement all non-hydrogen atoms for both structures were refined with anisotropic thermal displacement parameters. Hydrogen atoms were located directly from the Fourier map and their

(25) *Apex2*, v. 2.1-0; Bruker Nonius: Delft, The Netherlands, 2003−2004; Bruker AXS: Madison, WI, 2005−2006.
(26) (a) Sheldrick, G. M. *SADABS*; University of Göttingen: Göttingen, Germany, 1996. (b) *SAINT*, V7.34A; Bruker Nonius: Delft, The Netherlands, 2007.
(27) Blessing, R. H. *Acta Crystallogr.* **1995**, *A51*, 33–38.
(28) Kalinowski, J. *jdVis, a program for charge density properties visualization*; http://jak.kalinowscy.eu/jdvis.
(29) Sheldrick, G. M *Acta Crystallogr.* **1990**, *A46*, 467–473.
(30) Sheldrick, G. M. *SHELXL97, Program for the Refinement of Crystal Structures*; University of Göttingen: Göttingen, Germany, 1997.
(31) *International Tables for Crystallography*; Wilson, A. J. C., Ed.; Kluwer: Dordrecht, The Netherlands, 1992; Vol. *C*.

Table 2. Experimental Details

	1	2	3
formula	C12 H14 Fe	C20 H30 Fe	C14 H14 Fe O2
weight	214.08	326.29	270.10
system	monoclinic	orthorhombic	monoclinic
space group	*P*2(1)/*c*	*Cmca*	*P*2(1)/*c*
a [Å]	12.1498(2)	15.0905(10)	5.79960(10)
b [Å]	7.43250(10)	11.4741(8)	12.9042(3)
c [Å]	10.8095(2)	9.9484(6)	14.8381(4)
α [deg]	90.0	90.0	90.0
β [deg]	103.3860(10)	90.0	90.7290(10)
γ [deg]	90.0	90.0	90.0
V [Å^3]	949.62(3)	1722.6(2)	1110.38(4)
Z, density [g/cm^3]	4, 1.497	4, 1.258	4, 1.616
shape	planar	prismatic	planar
color	yellow	yellow	orange
size max., mid., min. [mm]	0.22, 0.16, 0.09	0.20, 0.20, 0.12	0.12, 0.08, 0.03
F000	448	704	560
μ [mm^{-1}]	1.532	0.868	1.342
temperature [K]	100(2)	90(2)	90(2)
R_{int}	0.0282	0.0226	0.0294
sin *θ*/*λ* [Å^{-1}]	1.08	1.13	1.16
completeness	0.990	0.978	0.974
N.refl	10118	5294	14275
N.refl > 2*σ*	8364	4431	11698
SHELX refinement			
N.par	174	84	188
R(*F*)	0.0217	0.0265	0.0313
R(*F*)all	0.0303	0.0337	0.0435
*wR*2	0.0597	0.0755	0.0784
GoF	1.023	1.138	1.071
highest peak/hole [e Å^{-3}]	0.868/−1.072	0.851/−0.691	2.048/−0.729
rms	0.071	0.073	0.100
multipole refinement			
sin *θ*/*λ* [Å^{-1}]	1.05	1.16	1.14
N.refl/N.par	7546/348	4334/199	11058/428
R(*F*)	0.013	0.019	0.021
R(*F*)all	0.023	0.029	0.043
*wR*2	0.015	0.023	0.024
GoF	1.178	2.658	1.439
highest peak/hole [e Å^{-3}]	0.242/−0.240	0.690/−0.389	0.448/−0.781
highest peak/hole (Fe^{2+}) [e Å^{-3}]	0.242/−0.240	0.293/−0.233	0.382/−0.320
rms	0.040	0.047	0.072

positions and isotropic thermal displacement parameters were refined against whole data sets. No extinction correction was needed.

Multipole Refinement. The program XDLSM of the package XD[32] was used for the purpose of multipole refinements. The Hansen−Coppens formalism[33] was applied, the atomic electron density being divided into three components:

$$\rho_k(r_k) = \rho_{core}(r_k) + P_{\text{valence}}\kappa^3\rho_{\text{valence}}(\kappa r_k) + \kappa'^3\sum_{l=0}^{l_{\max}} R_l(\kappa' r_k)\sum_{m=-l}^{+l} P_{lm\pm}\, d_{lm\pm}(\vartheta_k, \varphi_k)$$

(a) a spherically averaged free-atom Hartree−Fock core contribution, ρ_{core}; (b) a spherically averaged free-atom Hartree−Fock normalized to one electron valence contribution, ρ_{valence}, with refineable population parameter P_{valence} and the dimensionless expansion-contraction parameter κ; and (c) a deformation term expressed as normalized Slater-type radial function $R_l(\mathbf{r}_k)$ modulated by density normalized, real spherical harmonic angular functions $d_{\text{lm}\pm}(\vartheta,\varphi)$ defined on local axes centered on the atoms and with population parameters $P_{lm\pm}$. representing the deviation of the valence density from spherical symmetry, modified by the dimensionless expansion-contraction parameter κ'. Scattering factors for all atoms were derived from wave functions tabulated by Su and Coppens[34]. The atomic scattering factor was used for Fe in all refinements. The iron was initially assumed as neutral, and the population of the 4s orbital was assigned to the core and kept fixed. Local coordinate systems were defined for all atoms in a way that enabled application of symmetry constraints in the later stages of refinement. The general rule was that the local *Z*-axis for the metal ion should be perpendicular to the plane of the *η*-ligands, while the *X*-axis was located symmetrically with respect to the substituents. The ring C atoms were expected to obey local m symmetry where m would be the plane of the *η*-ligand, with *Z*-axis perpendicular to it. Similarly, multipole populations of oxygen atoms in compound **3** were constrained to obey local m symmetry where m would be the plane of the carbonyl moiety C-(C=O)-C, with the *Z*-axis perpendicular to it.

The carbon atoms in methyl groups were to obey 3 m symmetry with 3-fold axis (*Z*-axis) located along the C−C bond. In the case of compound **2**, the local coordinate systems were chosen to comply with the local crystallographic symmetry of the atoms in special positions (Fe(1)-mm2, C(1)-m, C(4)-m, H(4A)-m) and the *Z*-axis was set each time in a crystallographic [100] direction. The *X*-axis for iron was directed toward the Cp plane, analogously to the *Z*-axis in the case of remaining two structures.

The refinement with XDLSM of positional and thermal parameters of non-hydrogen atoms against a whole data set with a statistical weighting scheme was conducted for each of the three data sets. After it had reached convergence, we inspected the difference density maps. Well pronounced residuals indicating highly aspherical electron density distribution in the regions of bonds and around metal ions were observed in the case of all components. However, additional residual peaks were observed for the compounds **2** and **3** that could not be attributed to any structural features. Neither refinement statistics, nor the thermal displacement parameters in the structures, nor the peaks positions suggested any kind of structural disorder. Those sharp peaks were additionally visible only for high-order data, and disappeared thoroughly when the data with sin *θ*/*λ* > 0.9 Å^{-1} were excluded. A similar situation has been previously reported as an effect of extra Thermal Diffuse Scattering (TDS).[35] Because of its nature[36], the TDS contribution to a Bragg reflection does not depend on the resolution, whereas the X-ray scattering intensities diminish with the resolution. Therefore, mainly high-order data are affected by the TDS contribution. Another reason for the appearance of the peaks may be a scaling problem. Preliminary inspection of the charge density at BCPs and multipole populations in the vicinity of inexplicable high residual peaks showed that none of the properties were significantly affected, therefore whole data sets were applied in further analysis.

The fractal dimension[37] and normal probability plots[38] for all the data sets were examined in the next step. The plots are deposited as Figures **1S** and **2S** in the Supporting Information. According to those plots, statistical weights were retained for structures **1** and **3** throughout the rest of the refinement. A special

(32) Volkov, A.; Macchi, P.; Farrugia, L. J.; Gatti, C.; Mallinson, P.; Richter, T.; Koritsanszky, T. *XD2006, A Computer Program Package for Multipole Refinement, Topological Analysis of Charge Densities and Evaluation of Intermolecular Energies from Experimental and Theoretical Structure Factors*; 2006; http://xd.chem.buffalo.edu/.

(33) (a) Coppens, P. *X-Ray Charge Densities and Chemical Bonding*; Oxford University Press: New York, 1997. (b) Hansen, N. K.; Coppens, P. *Acta Crystallogr*. **1978**, *A34*, 909–921.

(34) Su, Z.; Coppens, P. *Acta Crystallogr*. **1998**, *A54*, 646.
(35) Ohba, S.; Sato, S.; Saito, Y. *Acta Crystallogr*. **1983**, *B39*, 49–53.
(36) Helmholdt, R. B.; Vos, A. *Acta Crystallogr*. **1977**, *A33*, 38–45.
(37) Meindl, K.; Henn, J. *Acta Crystallogr*. **2008**, *A64*, 404–418.
(38) Abrahams, S. C.; Keve, E. T. *Acta Crystallogr*. **1971**, *A27*, 157–165.

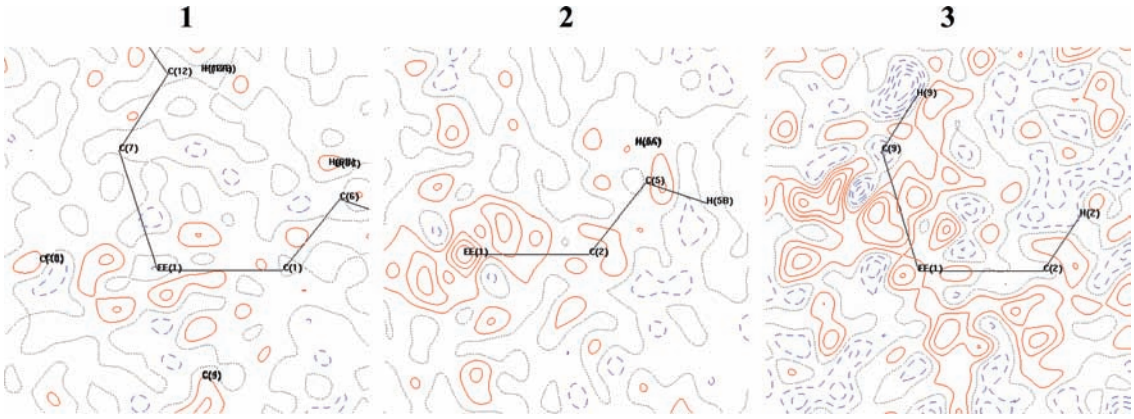

Figure 2. Residual density maps in the vicinity of iron for the analyzed compounds drawn against the data up to the 0.9 $Å^{-1}$ resolution. Contours drawn at 0.05 e $Å^{-3}$ intervals. Positive density indicated as red solid lines, negative as blue dashed lines, and zero contours drawn as gray dotted lines.

weighting scheme (calculated with the program XDRKplot[39]) where $w_1 = [F_o\text{sqrt}(w_2) + \text{sqrt}(F_o^2 w_2^2 + \text{sqrt}(w_2^2))]^2$ and $w_2 = 1/[s^2(F_o^2) + (0.02P)^2 + 0.15P]$ (where $P = 0.3333F_o^2 + 0.6667F_c^2$) was applied for data set **2** at the final refinement stage, (otherwise the scaling problems at the iron atom appeared, resulting in high residual peak at the exact iron position). The fact that the normal probability plot for this compound should be significantly different from ideal could be attributed to F super lattice constituted by Fe atoms in this highly symmetric structure.

The refinement was repeated against high-order data, that is, data for which $\sin\theta/\lambda > 0.7$, to obtain the most accurate starting structural parameters for multipole refinement. At the next step, the positional and thermal parameters for non-H atoms were fixed on the values obtained in refinement against high-order data. The C−H distances were constrained to the average values obtained for neutron diffraction experiments. The isotropic thermal displacement parameters for H atoms were refined against low-order data ($\sin\theta/\lambda < 0.8$), and such a model was converted into cif format and subjected to SHADE2[40] server to obtain estimated anisotropic displacement parameters (ADPs) for hydrogen atoms. The use of simulated ADPs for hydrogen atoms have already been shown to significantly improve the results of experimental charge density refinements[41]. Estimated ADPs for hydrogen atoms were incorporated into the model and kept fixed during the multipole refinements.

The remaining positional and thermal parameters were also fixed at the next refinement stage. Local symmetry constraints were applied to the multipole populations of selected atoms according to their closest environments (**1**, **3**) or crystallographic site symmetry (**2**). Chemical constraints were applied to H atoms: hydrogen atoms belonging to the same η-ligand or the same methyl group were forced to have similar multipolar populations. Separate κ, κ' were assigned for different elements and additionally for aromatic, carbonyl, and methyl carbon atoms.

The multipole refinements were conducted in stepwise manner, up to the hexadecapole level for non-H atoms and bond directed dipoles for hydrogen atoms. When the multipole populations converged, the kappa parameters were let to refine. At last the positional and thermal parameters of non-H atoms were refined with the multipole populations fixed. All the refinements converged satisfactorily, with max shift to standard deviation ratio going well below 10^{-7}. An attempt at the refinement of anharmonic thermal motion for Fe ion in the case of compound **1** resulted in unstable refinement and did not improve residual density maps, and therefore was abandoned. The summary of the refinement results for all three compounds is presented in Table 2. The residual density values around Fe^{2+} are in the case of all the compounds around ±0.3 e $Å^{-3}$, and the maps are featureless according to visual inspection and featurelessness tests made with the jnk2RDA program[37]. The fractal dimension plots are reported in the Supporting Information, Table 1S. The residual density maps for the compounds are presented in the Figure 2.

The Hirshfeld[42] test for covalent bonds gives the average values of 3, 1.6, and 1 [1.0^{-4} $Å^2$] for compounds **1**, **2**, and **3**, respectively. The highest observed value is 9 in the case of bonding of aromatic moiety with external substituent in **2** (C1−C4), **3** (C1−C6), and **3** (C1−C6). This suggests that the refinements were complete and atomic thermal motions well resolved in the case of all compounds.

The topological analysis of the charge density $\rho(r)$ and laplacian $\nabla^2\rho(r)$ were conducted with the XDPROP program of the XD package[32]. The estimation of d-orbital populations resulting from the multipolar charge density model has been also conducted using the XDPROP package, according to the method of Holladay et al.[43]. The kinetic energy densities $G(r_{BCP})$ at BCPs were estimated using the approximation of Abramov[44]:

$$G(r_{BCP}) = 0.3\left(\frac{3\pi}{2}\right)^{2/3}\rho(r_{BCP})^{5/3} + \frac{1}{6}\nabla^2(r_{BCP})$$

while the corresponding potential energy densities at BCP $V(r_{BCP})$ were obtained from the local virial theorem:

$$V(r_{BCP}) = \frac{1}{4}\nabla^2(r_{BCP}) - 2G(r_{BCP})$$

and the total energy density at BCP was estimated as $H(r_{BCP}) = G(r_{BCP}) + V(r_{BCP})$.

Theoretical single point calculations using the B3LYP density functional theory (DFT) functional and 6-311++G or Wachters-f[45] basis sets for light atoms and metal atoms accordingly were undertaken with GAUSSIAN03[46]. The calculations were conducted for the final experimental geometries of the analyzed molecules. Natural Population Analysis (NPA)[47,48] was conducted on the resulting wave functions. In particular, the populations of d-orbitals of iron resulting from multipole refinement were compared with "natural" d-orbital populations obtained from DFT calculations to have a reference state for the experimental results.

(39) Stash, A. *DRK Plot for XD 1.0*; 2004.
(40) Madsen, A. O. *J. Appl. Crystallogr.* **2006**, *39*, 757–758.
(41) Munshi, P.; Madsen, A. O.; Spackman, M. A.; Larsen, S.; Destro, R. *Acta Crystallogr.* **2008**, *A64*, 465.
(42) Hirschfeld, F. L.; Rabinovich, D. *Acta Crystallogr.* **1973**, *A29*, 510–513.
(43) Holladay, A.; Leung, P.; Coppens, P. *Acta Crystallogr.* **1983**, *A39*, 377–387.
(44) Abramov, Y. A. *Acta Crystallogr.* **1997**, *A53*, 264–272.
(45) Wachters, J. H. *J. Chem. Phys.* **1970**, *52*, 1033–1036.

Table 3. Fe−C and C−C Distances and Selected Angles for the Analyzed Compounds

	1		2		3
FE(1) C(1)	2.0580(3)	FE(1) C(1)	2.0533(4)	FE(1) C(1)	2.0302(4)
FE(1) C(2)	2.0448(3)	FE(1) C(2)	2.0542(3)	FE(1) C(2)	2.0461(3)
FE(1) C(3)	2.0421(3)	FE(1) C(3)	2.0520(2)	FE(1) C(3)	2.0644(4)
FE(1) C(4)	2.0412(3)			FE(1) C(4)	2.0660(4)
FE(1) C(5)	2.0471(2)			FE(1) C(5)	2.0411(4)
FE(1) C(7)	2.0551(3)			FE(1) C(8)	2.0358(4)
FE(1) C(8)	2.0407(2)			FE(1) C(9)	2.0454(4)
FE(1) C(9)	2.0417(2)			FE(1) C(10)	2.0650(4)
FE(1) C(10)	2.0464(3)			FE(1) C(11)	2.0555(4)
FE(1) C(11)	2.0500(3)			FE(1) C(12)	2.0491(3)
average	2.05		2.053		2.050
Fe cent1	1.647		1.651		1.649
Fe cent2	1.646		1.651		1.649
cent1 Fe cent2	178.40		180		178.87
ϕ angle	−3.62		35.96		−4.89 (139.70)
C(1) C(2)	1.4306(4)	C(1) C(2)	1.4374(4)	C(1) C(2)	1.4396(5)
C(1) C(5)	1.4294(4)	C(2) C(3)	1.4326(4)	C(1) C(5)	1.4387(5)
C(2) C(3)	1.4274(5)	C(3) C(3)	1.4315(6)	C(2) C(3)	1.4252(6)
C(3) C(4)	1.4257(5)			C(3) C(4)	1.4316(6)
C(4) C(5)	1.4286(4)			C(4) C(5)	1.4220(6)
C(7) C(8)	1.4289(4)			C(8) C(9)	1.4394(5)
C(7) C(11)	1.4322(4)			C(8) C(12)	1.4414(5)
C(8) C(9)	1.4298(4)			C(9) C(10)	1.4263(6)
C(9) C(10)	1.4291(4)			C(10) C(11)	1.4311(5)
C(10) C(11)	1.4287(4)			C(11) C(12)	1.4249(6)
average	1.428		1.434		1.427
C(1) C(6)	1.4905(4)	C(1) C(4)	1.4950(6)	O(1) C(6)	1.2274(6)
C(7) C(12)	1.4930(4)	C(2) C(5)	1.4936(5)	O(2) C(13)	1.2265(6)
		C(3) C(6)	1.4979(4)	C(1) C(6)	1.4722(5)
				C(8) C(13)	1.4745(6)
				C(6) C(7)	1.5034(6)
				C(13) C(14)	1.5079(6)
average C−CH3	1.49		1.5		1.51
				O(1) C(6) C(1) C(2)	−11.73
				O(2) C(13) C(8) C(9)	8.50

The method is based on the construction of a set of "natural atomic orbitals" (NAOs) for a given molecule. In the molecular case, NAOs are the orthonormal, single atom centered orbitals of maximal occupancy for a given wave function. As NAOs form an orthonormal set, completely spanning the space of basis orbitals, their populations sum up to the total number of electrons in the system. NAOs are also intrinsic to the wave function rather than to a particular basis set and are found to converge toward well-defined limits with the improvement of a basis set, with stable populations. The advantages of the NAOs, apart from the relative independence from a basis set are the proven usefulness in description of charge distribution in metal containing compounds and the possibility of a direct comparison between the orbital populations of NAOs with the orbital populations derived from experimental charge density studies, in particular, the d-orbital populations of the transition metals.

Results and Discussion

Structural Comparisons. All three compounds crystallize in centrosymmetric space groups, without solvent, and contain no more than one independent molecule of the compound in the crystallographic asymmetric unit. The most important geometrical parameters for the structures studied are given in Table 3.

Compound **1** displays a conformation close to eclipsed (φ angle of −3.62), with methyl arms located one above another (φ angle defined as a relative rotation of two Cp rings, analogously to literature[49]). The Cp rings are nearly

(46) Frisch, M. J.; Trucks, G. W.; Schlegel, H. B.; Scuseria, G. E.; Robb, M. A.; Cheeseman, J. R.; Montgomery, Jr., J. A.; Vreven, T.; Kudin, K. N.; Burant, J. C.; Millam, J. M.; Iyengar, S. S.; Tomasi, J.; Barone, V.; Mennucci, B.; Cossi, M.; Scalmani, G.; Rega, N.; Petersson, G. A.; Nakatsuji, H.; Hada, M.; Ehara, M.; Toyota, K.; Fukuda, R.; Hasegawa, J.; Ishida, M.; Nakajima, T.; Honda, Y.; Kitao, O.; Nakai, H.; Klene, M.; Li, X.; Knox, J. E.; Hratchian, H. P.; Cross, J. B.; Bakken, V.; Adamo, C.; Jaramillo, J.; Gomperts, R.; Stratmann, R. E.; Yazyev, O.; Austin, A. J.; Cammi, R.; Pomelli, C.; Ochterski, J. W.; Ayala, P. Y.; Morokuma, K.; Voth, G. A.; Salvador, P.; Dannenberg, J. J.; Zakrzewski, V. G.; Dapprich, S.; Daniels, A. D.; Strain, M. C.; Farkas, O.; Malick, D. K.; Rabuck, A. D.; Raghavachari, K.; Foresman, J. B.; Ortiz, J. V.; Cui, Q.; Baboul, A. G.; Clifford, S.; Cioslowski, J.; Stefanov, B. B.; Liu, G.; Liashenko, A.; Piskorz, P.; Komaromi, I.; Martin, R. L.; Fox, D. J.; Keith, T.; Al-Laham, M. A.; Peng, C. Y.; Nanayakkara, A.; Challacombe, M.; Gill, P. M. W.; Johnson, B.; Chen, W.; Wong, M. W.; Gonzalez, C.; and Pople, J. A. *Gaussian 03*, Revision C.02; Gaussian, Inc.: Wallingford, CT, 2004.

(47) Reed, A. E.; Weinstock, R. B.; Weinhold, F. *J. Chem. Phys.* **1985**, *83*, 735–746.

(48) Weinhold, F.; Landis, C. F. *Chem. Educ.: Theory and Practice in Europe* **2001**, *2*, 91–104.

(49) Tanjaroon, C.; Keck, K. S.; Kukolich, S. G. *J. Am. Chem. Soc.* **2004**, *126*, 844–850.

Table 4. List of BCPs, Charge Densities, Laplacians, Ellipticities and Energy Densities for (a) **1**, (b) **2**, and (c) **3**

(a) **1**	$\rho(r_{BCP})$ [e Å^{-3}]	$\nabla^2\rho(r_{BCP})$ [e Å^{-5}]	ellipticity	$G(r_{BCP})$ [Ha a_0^{-3}]	$V(r_{BCP})$ [Ha a_0^{-3}]	$H(r_{BCP})$ [Ha a_0^{-3}]	$G(r_{BCP})/\rho(r_{BCP})$ [Ha e^{-1}]	$\lvert V(r_{BCP})\rvert/G(r_{BCP})$
FE(1)−C(1)	0.552(7)	6.80(1)	3.45	0.091	−0.112	−0.021	1.116	1.227
FE(1)−C(2)	0.551(6)	7.05(1)	3.45	0.093	−0.113	−0.02	1.137	1.213
FE(1)−C(3)	0.555(6)	7.64(1)	14.67	0.097	−0.116	−0.018	1.185	1.187
FE(1)−C(4)	0.555(6)	7.64(1)	14.67	0.097	−0.116	−0.018	1.185	1.187
FE(1)−C(5)	0.555(6)	7.30(1)	4.95	0.095	−0.115	−0.019	1.157	1.204
FE(1)−C(7)	0.572(7)	6.87(1)	2.25	0.094	−0.118	−0.023	1.114	1.246
FE(1)−C(9)	0.582(6)	7.17(1)	3.23	0.098	−0.121	−0.024	1.135	1.241
FE(1)−C(11)	0.543(6)	7.29(1)	4.16	0.093	−0.111	−0.018	1.162	1.191
C(1)−C(2)	1.95(2)	−15.65(5)	0.23	0.254	−0.671	−0.417	0.88	2.638
C(1)−C(5)	2.00(2)	−17.05(5)	0.29	0.261	−0.699	−0.438	0.88	2.678
C(2)−C(3)	1.98(2)	−16.70(7)	0.24	0.257	−0.687	−0.43	0.875	2.675
C(3)−C(4)	2.03(2)	−17.96(6)	0.26	0.263	−0.712	−0.449	0.874	2.709
C(4)−C(5)	1.96(2)	−14.94(5)	0.24	0.262	−0.678	−0.416	0.902	2.593
C(7)−C(8)	1.97(2)	−15.38(5)	0.26	0.263	−0.686	−0.423	0.901	2.606
C(7)−C(11)	1.97(2)	−16.36(5)	0.25	0.256	−0.682	−0.426	0.877	2.663
C(8)−C(9)	1.96(2)	−15.09(5)	0.18	0.262	−0.681	−0.419	0.902	2.597
C(9)−C(10)	1.96(2)	−16.29(5)	0.27	0.254	−0.678	−0.423	0.874	2.664
C(10)−C(11)	1.98(2)	−15.85(5)	0.21	0.264	−0.692	−0.428	0.897	2.624
C(1)−C(6)	1.76(2)	−14.05(4)	0.01	0.209	−0.565	−0.355	0.802	2.696
C(7)−C(12)	1.74(1)	−13.73(4)	0.05	0.206	−0.555	−0.349	0.798	2.691

(b) **2**	$\rho(r_{BCP})$ [e Å^{-3}]	$\nabla^2\rho(r_{BCP})$ [e Å^{-5}]	ellipticity	$G(r_{BCP})$ [Ha a_0^{-3}]	$V(r_{BCP})$ [Ha a_0^{-3}]	$H(r_{BCP})$ [Ha a_0^{-3}]	$G(r_{BCP})/\rho(r_{BCP})$ [Ha e^{-1}]	$\lvert V(r_{BCP})\rvert/G(r_{BCP})$
FE(1)−C(1)	0.581(7)	7.16(2)	1.39	0.098	−0.121	−0.023	1.135	1.24
FE(1)−C(2)	0.57(1)	7.20(2)	2	0.096	−0.117	−0.021	1.143	1.223
FE(1)−C(3)	0.55(1)	7.02(2)	7.21	0.093	−0.112	−0.02	1.135	1.213
C(1)−C(2)	2.00(1)	−16.17(2)	0.2	0.266	−0.7	−0.434	0.898	2.63
C(1)-X8_C(2)	2.00(3)	−16.17(7)	0.2	0.266	−0.7	−0.434	0.898	2.63
C(2)−C(3)	1.97(2)	−15.78(6)	0.25	0.261	−0.686	−0.425	0.892	2.627
C(3)-X8_C(3)	1.98(2)	−16.48(9)	0.35	0.257	−0.686	−0.428	0.878	2.664
C(1)−C(4)	1.87(2)	−16.76(5)	0.04	0.222	−0.618	−0.396	0.802	2.782
C(2)−C(5)	1.85(2)	−15.57(6)	0.01	0.225	−0.612	−0.387	0.821	2.716
C(3)−C(6)	1.75(2)	−12.12(6)	0.07	0.219	−0.564	−0.345	0.845	2.573

(c) **3**	$\rho(r_{BCP})$ [e Å^{-3}]	$\nabla^2\rho(r_{BCP})$ [e Å^{-5}]	ellipticity	$G(r_{BCP})$ [Ha a_0^{-3}]	$V(r_{BCP})$ [Ha a_0^{-3}]	$H(r_{BCP})$ [Ha a_0^{-3}]	$G(r_{BCP})/\rho(r_{BCP})$ [Ha e^{-1}]	$\lvert V(r_{BCP})\rvert/G(r_{BCP})$
FE(1)−C(1)	0.629(8)	8.24(2)	4.79	0.112	−0.139	−0.027	1.201	1.237
FE(1)−C(2)	0.611(8)	7.38(2)	8.9	0.103	−0.13	−0.027	1.143	1.26
FE(1)−C(4)	0.620(8)	7.52(2)	4.32	0.106	−0.133	−0.028	1.151	1.262
FE(1)−C(5)	0.622(8)	7.92(2)	6.65	0.109	−0.135	−0.027	1.18	1.245
FE(1)−C(8)	0.632(8)	7.53(2)	7.43	0.108	−0.137	−0.029	1.148	1.273
FE(1)−C(9)	0.636(8)	7.28(2)	6.19	0.106	−0.137	−0.031	1.129	1.29
FE(1)−C(12)	0.616(8)	6.79(2)	3.44	0.1	−0.13	−0.03	1.096	1.296
C(1)−C(2)	1.94(2)	−14.41(6)	0.21	0.261	−0.672	−0.411	0.907	2.572
C(1)−C(5)	1.92(2)	−13.83(6)	0.3	0.259	−0.661	−0.402	0.908	2.555
C(2)−C(3)	1.98(2)	−15.36(6)	0.19	0.264	−0.688	−0.424	0.903	2.603
C(3)−C(4)	1.89(2)	−13.32(6)	0.2	0.253	−0.644	−0.391	0.902	2.546
C(4)−C(5)	2.01(2)	−14.13(6)	0.28	0.284	−0.714	−0.43	0.953	2.516
C(8)−C(9)	1.94(2)	−13.47(6)	0.28	0.265	−0.67	−0.405	0.924	2.527
C(8)−C(12)	1.90(2)	−14.26(6)	0.17	0.25	−0.647	−0.398	0.885	2.593
C(9)−C(10)	1.90(2)	−12.80(6)	0.24	0.26	−0.652	−0.392	0.921	2.511
C(10)−C(11)	1.99(2)	−15.34(6)	0.3	0.269	−0.698	−0.428	0.913	2.591
C(11)−C(12)	2.01(2)	−16.04(6)	0.27	0.269	−0.705	−0.436	0.906	2.618
O(1)−C(6)	2.89(4)	−17.8(3)	0.15	0.577	−1.339	−0.762	1.346	2.32
O(2)−C(13)	2.77(4)	−9.5(2)	0.1	0.586	−1.271	−0.685	1.426	2.169
C(1)−C(6)	1.88(2)	−15.58(6)	0.16	0.234	−0.63	−0.396	0.839	2.691
C(8)−C(13)	1.89(2)	−16.66(6)	0.12	0.23	−0.633	−0.403	0.82	2.751
C(6)−C(7)	1.76(2)	−14.85(5)	0.03	0.203	−0.559	−0.357	0.778	2.76
C(13)−C(14)	1.74(2)	−12.01(5)	0.15	0.218	−0.561	−0.343	0.844	2.571

parallel, and the angle between vectors connecting iron to the centroids of the Cp rings differs from 180° only by 1.6°. According to Tanjaroon et al.[49] this is one of the two conformations experimentally observed for the species, and the only one that has ever been observed in solid state, although theoretical DFT calculations for an isolated molecule suggest that this conformation is not the most energetically stable. The current structure stays in good agreement with data obtained previously at higher temperatures.

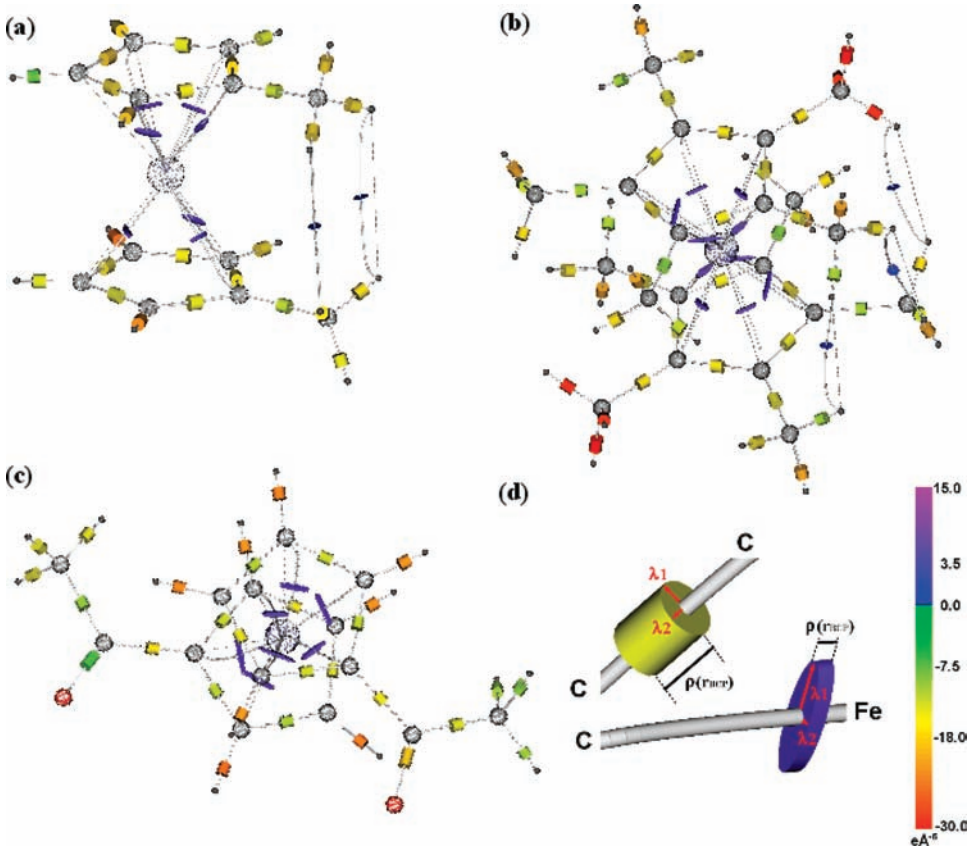

Figure 3. Visualizations of the bond paths and BCPs for the analyzed compounds (a) **1**, (b) **2**, and (c) **3** and (d) explanation of the graphical representation. The bond paths are presented as gray lines. The BCPs are represented as cylinders. The length of the cylinder is scaled by $\rho(r_{BCP})$, while its crossections illustrate ellipticity at BCP and color denotes the value of $\nabla^2\rho(r_{BCP})$ (violet, positive; green to red, negative; scale from -30.0 to $+15.0$ e Å^{-5}). In cases (a) and (b), bond paths connecting hydrogen atoms from opposing methyl groups have also been plotted[28].

Compound **2** is an example of ideally staggered geometry, with C_{2h} symmetry of the molecule and Fe atom located on the crystallographic inversion center. Apart from iron, the C(1), C(4), and H(4A) atoms occupy special positions on a m mirror plane. The structure at 100 K agrees with previously determined ones, obtained at higher temperatures, up to such a detail as the orientation of hydrogen atoms in methyl groups with respect to the Cp rings. However, the average $C_{ring}-C_{methyl}$ distance obtained in current study is longer by 0.015 Å than a distance reported previously (1.419 Å). It is also by 0.01 Å longer than similar distances in remaining two compounds. Among the three analyzed compounds, this one also displays the longest distance from central metal ion to the Cp ring centroid.

Compound **3** conformation is again close to eclipsed. The two acetyl moieties differ in conformation, oxygen O(1) being rotated slightly above the adjacent Cp plane and away from Fe, whereas O(2) is inclined toward the inside of the molecular sandwich, a feature already observed in high temperature studies. The carbonyl moieties show nevertheless some degree of conjugation with Cp rings, as the $C_{Cp}-C_{CO}$ bond distance is significantly shorter than a formally single C−C bond.

The different influence of the methyl and acetyl substituents on the Cp rings interactions with iron manifests itself in the Fe−C distances. In the case of dimethyl ferrocene, the Fe−C distances to substituted carbons are longer by 0.01 Å, whereas in the case of diacetyl ferrocene they are shorter by 0.01 Å.

The view along the [010] crystallographic direction indicates, that molecules of **1** form layers parallel to the 101 plane. Inside such a layer, the molecules pack so that the hydrogen atoms attached to Cp rings are directed toward the carbons from neighboring Cp rings, yielding a number of short C−H···C contacts. In a chosen layer, all methyl substituents are pointing in the same direction. The two neighboring layers are oriented either methyl to methyl or Cp to Cp, resulting in a number of short H···H contacts formation.

Columns of molecules stretching along the [011] crystallographic direction are the main packing motif of structure **2**. In a column, adjacent molecules are rotated by 90 degrees so that the methyl substituents are directed toward the Cp planes. The columns form layers perpendicular to 100, so as to maximize the number of C_{methyl}-H···C_{Cp} contacts.

The different orientation of two carbonyl moieties in the case of **3** leads to a different network of short C−H···O contacts around those two atoms. The main packing motif consists of layers of molecules perpendicular to the [010] crystallographic direction. In a layer, the molecules are slightly inclined with respect to the plane, thus enabling the O(1) and H(2) atoms to point into the middle of the neighboring sandwich complex, and form a number of short, nearly equidistant contacts with H(5)

and H(11) hydrogen atoms (packing diagrams in the Supporting Information, Figure S3).

Topological Charge Density Analysis. The general features of metal−ligand interactions are similar in the case of all three compounds. The values of $\rho(r_{BCP})$ and $\nabla^2\rho(r_{BCP})$, gathered in Table 4 (Figure 3), illustrate the differences between the Fe−C and C−C bonding. The Fe−C bonds are in all three cases characterized by positive and relatively small value of the laplacian. The values of $\rho(r_{BCP})$ and $\nabla^2\rho(r_{BCP})$ are similar in all three molecules, although their absolute values tend to be higher in the case of compound **3**, indicating stronger metal−ligands interactions. Not all possible BCPs were found for the compounds **1** and **3**. This problem has already been mentioned by Farrugia et al.[11] and explained as resulting from the relative flatness of the charge density function in the region of such interactions, leading to the meeting of BCPs and RCPs (so-called catastrophe).

The kinetic and potential energy densities derived from the properties of $\rho(r_{BCP})$ are also indicators of the variety of bonding interactions in the presented structures. The total energy densities obtained for Fe−C bonds conform well with the study by Farrugia et al.[11] The average values are small (−0.02 hartree/bohr^3) in the case of iron−carbon bonds, −0.35 hartree/bohr^3 for an average single C−C bond, −0.42 hartree/bohr^3 for delocalized C−C bond in Cp ring, and −0.71 hartree/bohr^3 for a formally double carbonyl bond.

The metal−ligand interactions can be classified as intermediate between the covalent, shared shell-type interactions and ionic, closed shell interactions. The positive values of $\nabla^2\rho(r_{BCP})$ and high ratios of $G(r_{BCP})/\rho(r_{BCP})$, exceeding 1.0, are characteristic for non-covalent interactions; there is significant amount of kinetic energy per electron present in these regions, indicating lower stability of such bonds. On the other hand, total energy density at BCPs is decidedly negative in all three ferrocene derivatives, and the ratio of potential to kinetic energy densities at BCPs falls in the range between 1 and 2. According to Gatti[50], such combination of charge density properties at BCPs suggest intermediate type of interactions, with some degree of covalency, measured as a $H(r_{BCP})/\rho(r_{BCP})$ ratio.

The π character of the bond in cyclopentadienyl rings is best illustrated by the deformation density or laplacian cross sections perpendicular to the bonds, which are decidedly elliptical. There is apparent deformation of the charge density around the ligand atom in the direction of the metal. Small charge concentrations can be observed at carbons from Cp rings, pointing toward the central iron atom (Figure 4).

On the other hand, the cross sections of the laplacian in all three structures show well shaped charge concentrations at the metal atom in the direction toward the centers of Cp ligands and away from metal−ligand vectors.

In the case of **3** there is particularly interesting enhancement of the charge density at BCPs of C(4)−C(5) and C(11)−C(12) bonds, which are both located "trans" with respect to the carbonyl oxygen atom. There is also a difference in $\rho(r_{BCP})$ and in the $\nabla^2\rho(r_{BCP})$ and therefore strength of the C−O bonds in the moiety, indicative of different intermolecular interactions in which the oxygen atoms are involved.

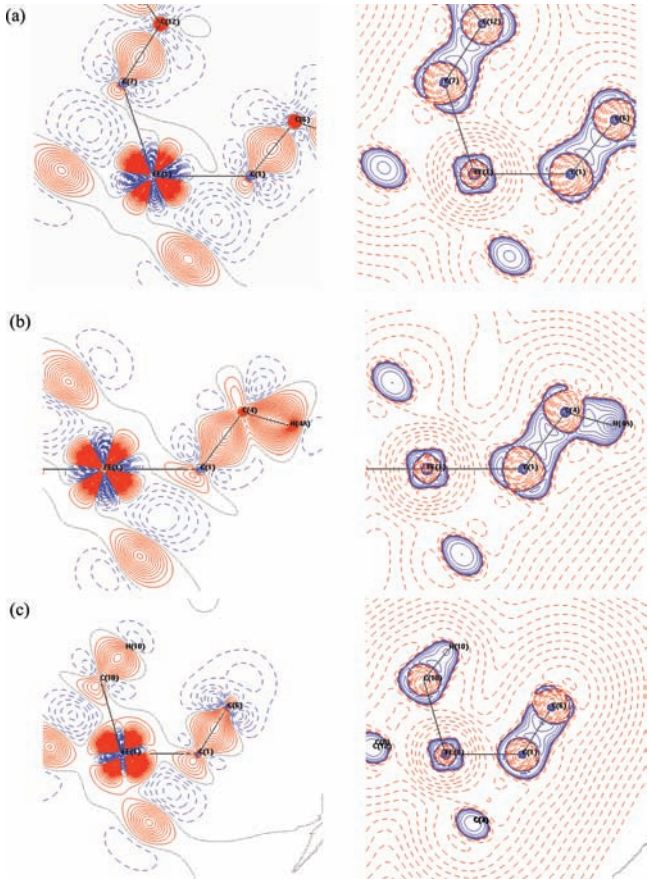

Figure 4. Examples of deformation density maps and laplacian cross sections for (a) **1**, (b) **2**, and (c) **3**. Contours for deformation density maps drawn at 0.05 e Å^{-3} intervals. Positive density indicated as red solid lines, negative ones as blue dashed lines, and zero contours drawn as gray dotted lines. In the case of laplacians, contours are on a geometric scale; a negative laplacian is indicated as blue solid lines, a positive one as red dashed lines.

Fe Species Characteristics. The properties of the iron in the η5-sandwich complexes may be described in terms of the calculated d-orbitals populations (Table 5), the deformation density, or laplacian distributions and atomic charges. A few features are common for all compounds.

One of the common features of the experimental charge densities of all three compounds is the total d-orbital population exceeding the formal count of 6 electrons. The excess negative charge seems to come from the carbon ligands, donating some of their density into the unoccupied orbitals around iron. The amount of the excess charge in the experimental charge density models depends on the character of the substituents in a given ferrocene derivative. On the other hand, the total d-orbital populations resulting from NPA analysis are very similar for all three compounds and do not follow the same order. This suggest, that differences in the experimental populations may be partly attributed to differences in the refinement models, that is, refined κ parameters and scale factors.

The populations of d-orbitals estimated on the basis of multipole parameters stay in agreement with the ligand field theory, as they clearly illustrate a split of d-orbitals into two distinct groups. Orbitals d_{z^2}, $d_{x^2-y^2}$, and d_{xy} in the

(50) Gatti, C. *Z. Kristallogr.* **2005**, *220*, 399–457.

Table 5. d-Orbital Populations for Fe in the Analyzed Compounds According to Multipole Refinement and Natural Population Analysis (NPA)[47,48]

	1 [e]	%	NPA	%	**2** [e]	%	NPA	%	**3** [e]	%	NPA	%
z^2	*1.64(1)*	*27,1*	*1.92*	*25.6*	*1.58(1)*	*24,3*	*1.67*	*22.1*	*2.03(2)*	*29,5*	*1.78*	*23.8*
xz	0.75(1)	12,4	0.94	12.5	*1.56(1)*	*24,0*	*1.56*	*20.7*	0.96(2)	13,9	1.26	16.8
yz	0.79(1)	13,1	0.96	12.8	0.98(1)	15,1	1.33	17.6	0.94(2)	13,6	1.12	15.0
$x^2 - y^2$	*1.40(1)*	*23,1*	*1.82*	*24.3*	*1.64(1)*	*25,2*	*1.86*	*24.6*	*1.65(2)*	*23,9*	*1.72*	*23.0*
xy	*1.46(1)*	*24,1*	*1.86*	*24.8*	0.74(1)	11,4	1.13	15.0	*1.31(2)*	*19,0*	*1.60*	*21.4*
tot d-pop	**6.05(1)**		7.50		**6.50(1)**		7.55		**6.89(2)**		7.48	

case of **1** and **3** or d_{z^2}, d_{xz}, and $d_{x^2-y^2}$ in the case of **2** are preferentially occupied, with populations well above 1e and above 20% of the total d-orbital population. These are the orbitals directed in between the carbon ligands (a_{1g} and e_{2g} symmetry representations in this coordinate system). The orbitals oriented along the main axis of the ferrocene moiety (i.e., the axis connecting the centroids of the Cp rings), namely, d_{z^2} in the case of **1** and **3** and $d_{x^2-y^2}$ of **2**, are the most populated and hence preferentially occupied, although the split between the populations is the most pronounced in **3** and very small in **2**. The populations of the next two most occupied orbitals are nearly equal in the case of methyl-substituted derivatives, whereas they differ significantly in the case of acetyl substituents. Interestingly, the preferred occupancy of the d_{z^2} orbital of a_{1g} symmetry disagrees with the energy order of the d orbitals present in literature [51,52], according to which the a_{1g} level should be slightly higher than e_{2g}, and, therefore, the occupancies would be expected to be biggest at d orbitals belonging to e_{2g} representation. The remaining orbitals, directed toward the coordinating carbons, show the populations smaller than 1e, not exceeding 15% of the total d-orbital population (e_{1g} symmetry representation). It is in agreement with the energy split of d orbitals in pseudo-octahedral ligand field generated by Cp ligands.

Such a distribution of d-electrons results in a characteristic shape of the positive deformation density, illustrated in the Figure 5. The positive electron density tends to occupy a space similar to that enclosed by a $3d_{z^2}$ orbital as calculated for isolated atom, with two maxima pointing toward the centroids of Cp rings and a torus of positive density located parallel to the Cp planes. A similar shape is enclosed by the outer isosurface of $\nabla^2\rho(r) = 0$, interpreted as a border of inner shells of metal atom.

Atomic Charges. There are differences in the final atomic charges (and contraction/expansion parameters) of Fe in the three compounds, disagreeing with the known electrochemical order. The monopole charge of iron in **2** (Table 6) is by 0.5e more negative than in **1**, and carries nearly −0.9e charge in the compound **3**. The iron charge resulting from multipole population analysis is always negative. The sign of the monopole charge of Fe is in general agreement with NPA, although the differences arising between the molecules are very small in the case of theoretical calculations. The Bader charge for iron is positive in compounds **1** and **3**, but negative for compound **2**.

The charges accumulated on Cp rings follow the same trend as the charges on iron. The cyclopentadienyl rings in **1** accumulate the most negative charge, reaching −0.1e in the case of the C(7)−C(11) group. In the case of **2** the charge concentrated on a ring is 0.24e, while for **3** it is on average 0.48e. The atomic charges, derived from monopole populations or integration of experimental charge density over atomic basins, and summed over the more important moieties, Cp-rings, methyl groups, and acetyl groups for **1**−**3** are shown in Table 6 and compared with theoretical NPA charges. None of the methods of atomic charge calculations yields charges that correlate with the formal oxidation potentials of the analyzed compounds (Figure 6).

The methyl groups in **1** and **3** tend to act as electron donors and adopt a positive sum of atomic charges, although the values of total charge differ from near zero in the case of C(5) in **2** to around 0.4e in the case of C(7) in **3**. On the contrary, carbonyl moieties in **3** act like electron acceptors and adopt negative total charges, withdrawing electron density from both Cp rings and neighboring

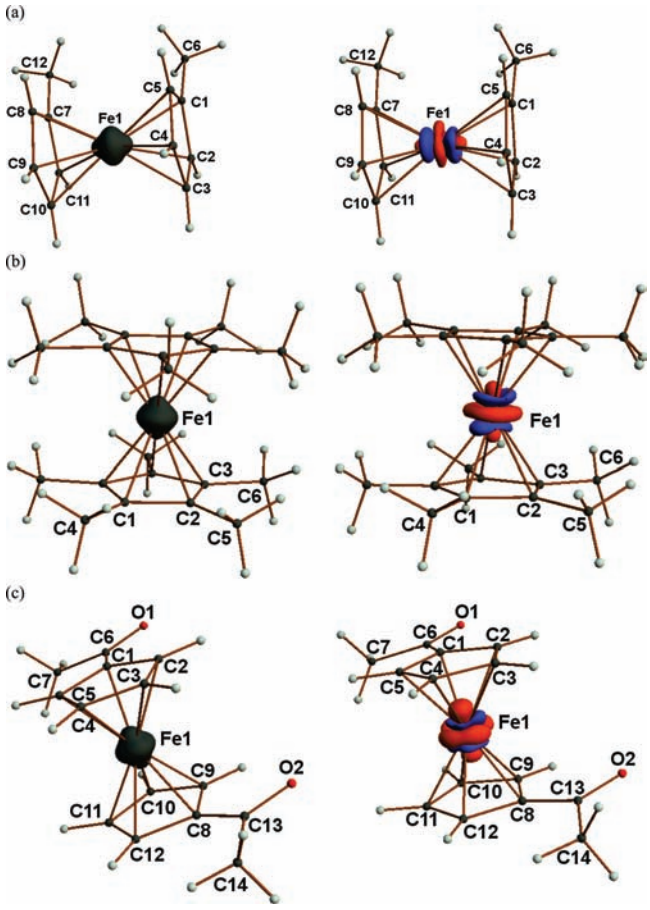

Figure 5. 3D laplacians and deformation density maps for (a) **1**, (b) **2**, and (c) **3**. The gray isosurfaces are drawn at the value of $\nabla^2\rho(r) = 0$. The deformation density isosurfaces have been drawn at +0.5 e Å^{-3} (red) and −0.5 e Å^{-3} (blue) density levels.

(51) Jean, Y. *Molecular Orbitals of Transition Metal Complexes*; Oxford University Press, New York, 2005.
(52) Neuse, E. W. *J. Inorg. Organomet. Polym. Mater.* **2005**, *15*, 1.

Table 6. Atomic Charges Summed over the More Important Moieties: Cp-Rings, Methyl Groups, and Acetyl Groups for (a) **1**, (b) **2**, and (c) **3**[a]

(a) charge [e]	multipole	Bader	NPA
Fe	−0,05	0,65	−0,41
ring C(1)−C(5)	0,02	−0,45	0,05
ring C(7)−C(11)	−0,10	−0,53	0,05
av	−0,04	−0,49	0,05
methyl C(6)	0,05	0,11	0,16
mehtyl C(12)	0,08	0,15	0,16
av	0,06	0,13	0,16
Ferrocene moiety	−0,13	−0,33	−0,31
(b) charge [e]	multipole	Bader	NPA
Fe	−0,49	−0,33	−0,37
ring C(1)−C(3)	0,24	−0,47	−0,03
methyl C(4)	−0,08	0,11	0,04
methyl C(5)	0,11	0,11	0,04
methyl C(6)	−0,07	0,01	0,04
av	−0,01	0,08	0,04
Ferrocene moiety	−0,01	−1,26	−0,43
(c) charge [e]	multipole	Bader	NPA
Fe	−0,89	0,14	−0,39
ring C(1)−C(5)	0,49	−0,11	0,13
ring C(8)−C(12)	0,47	−0,08	0,19
av	0,48	−0,09	0,16
carbonyl C(6)−O(1)	−0,24	−0,30	−0,02
carbonyl C(13)−O(2)	−0,27	−0,34	−0,02
methyl C(7)	0,39	0,45	0,03
methyl C(14)	0,05	0,23	0,07
av	0,22	0,34	0,05
actetal C(6)−C(7)	0,15	0,15	0,02
actetal C(13)−C(14)	−0,22	−0,12	0,05
av	−0,04	0,02	0,03
Ferrocene moiety	0,07	−0,05	−0,07

[a] Summations for a chosen moiety included hydrogen atoms bound directly to the carbons belonging to this moiety.

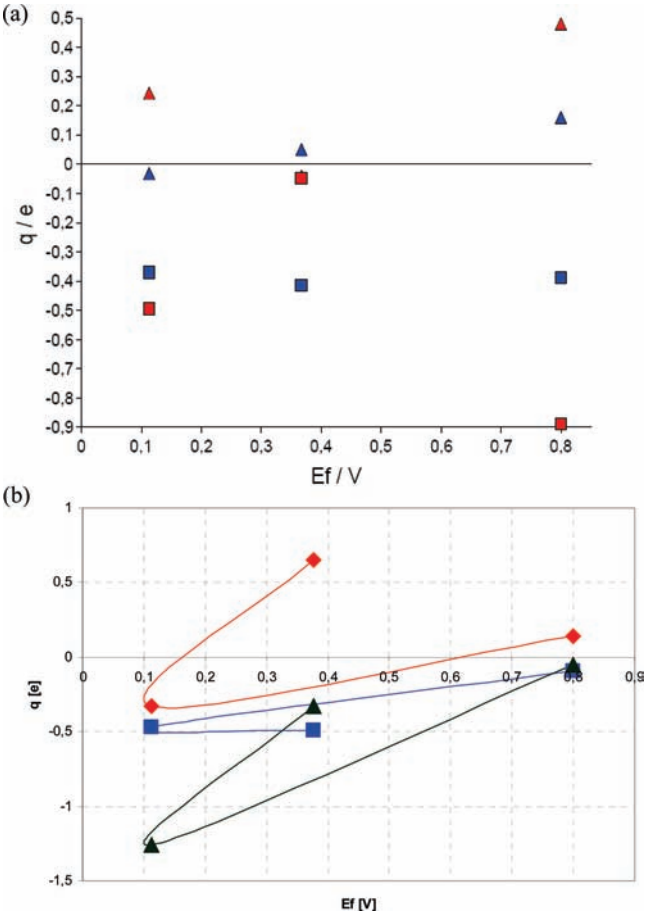

Figure 6. (a) Charges derived from monopole populations (red) and NPA (blue) for iron atoms (squares) and Cp rings (triangles) accordingly, presented versus formal oxidation potentials of the analyzed compounds (0.376 V for **1**, 0.113 V for **2**, and around 0.800 V for **3**) (b) Charges for iron (red), Cp rings (blue), and a whole ferrocene moiety (green), integrated over atomic basins and presented versus formal oxidation potentials of the analyzed compounds (0.376 V for **1**, 0.113 V for **2**, and around 0.800 V for **3**).

methyl groups. The negative charge concentrated on the oxygen atoms is quite significant, in agreement with its high expected electronegativity. The situation is different for **2** compound, where some methyl groups gather slightly negative monopole charge, although the value is close to zero. This may be due to the high symmetry of the molecule and the counterbalancing of the effects of single methyl groups on the Cp rings. It is also apparent that the methyl group localized in a special position, namely, C(4) in **2**, is the worst modeled group of all. Thus the properties calculated for this group are the least reliable (Figure 7).

The molecular dipole moments calculated for the compounds **1** and **3** are systematically larger by about 5 D in the case of experimental charge density analysis with respect to theoretical calculations for isolated molecules. They are equal to 5.2 D and 0.6 D for the multipole and SCF calculated dipole moments of **1**, 0 D for **2**, and 10.2 D (multipole) and 6.5 D (SCF) for **3**, respectively. The experimental dipole moment for **3** is equal to 4.23 D.[53]

Weak Interactions in Charge Density Point of View. For all short C−H···C and H···H contacts distinguished by geometrical criteria, BCPs have been found, and bond paths have been identified. Those interactions are weak and the $\rho(r_{BCP})$ values are on the same level of magnitude as rms residual density, which suggest they are to be treated with care. Nevertheless, the existence of bond paths confirms the meaningfulness of such interactions. The total energy density values at those BCPs are positive. Therefore the interactions may be classified as closed-shell, and formed in response to the close proximity of the atoms resulting from electrostatic interactions in crystal lattice. C−H···π interactions, namely, C(2)−H(2)···C(9) and C(6)−H(6B)···C(7), do not differ significantly from H···H interactions in terms of $\rho(r_{BCP})$ or energy density values (Table 7). Each hydrogen in the structure is involved in some kind of weak interaction.

Two H···H bonds, with well-defined BCPs and bond paths (Figure 3), connect the hydrogen atoms from the eclipsed methyl groups (H(12B)-H(6B) and H(12A)-H(6C)). The interactions are weak and of closed shell type (positive laplacians and $H(r_{BCP})$). However, interactions of similar nature, showing comparable values of energy densities at H−H BCPs, were investigated by means of theoretical calculations and described in detail by Matta et al.[54] in the case of nine hydrocarbon compounds. The study provided evidence, that such "H−H bonding" can

(53) Richmond, H. H.; Freiser, H. *J. Am. Chem. Soc.* **1954**, *77*, 2022–2023.

(54) Matta, C. F.; Hernandez-Trujillo, J.; Tang, T.-H.; Bader, R. F. W. *Chem.—Eur. J.* **2003**, *9*, 1940–1951.

provide a stabilizing contribution to the total energy of a molecule, even though the total energy densities at BCPs associated with these interactions are positive. The preference for the eclipsed conformation of compound **1** in the crystal structure may be therefore attributed at least partially to the stabilizing influence of the "H−H" bonding.

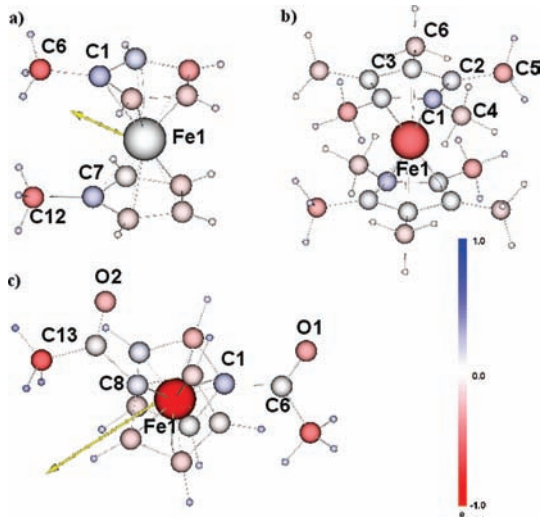

Figure 7. Atomic charge distributions derived from monopole populations for the analyzed compounds (a) **1**, (b) **2**, and (c) **3**. Negative charge represented in red, positive charge in blue, and zero charge in white. Scale from −1.0 to 1.0 e. The resulting dipole moment is presented as a yellow arrow, anchored at the molecules' center of mass and scaled in [D].

Interactions similar to those described in the case of dimethyl ferrocene, confirmed by the existence of H···H BCPs and bond paths between the methyl groups attached to opposite Cp rings, are observed in the structure of **2**. The intermolecular short contacts are in this case dominated by H···H interactions, presenting a variety of strengths. H(4A) hydrogen is involved in a sole interaction with C(3) carbon from the Cp ring of a neighboring molecule, for which a bond path can also be found. This may be an additional explanation for the atomic charge of the C(4) methyl group, different from the charges of the remaining methyl carbons in the compound **2**, as C(4) is involved in different kind of the intermolecular interactions.

The H(2) in the structure of **3** is directed in between the Cp rings of the neighboring molecule, related by translation along [100] direction. The short (3.302(2)Å) Fe···H distance suggests a weak electrostatic interaction of the hydrogen with the electron density of the Fe d orbitals; a case of such interaction, associated with the existence of a bond path, was recently reported by Borissova et al.[55] However, no bond path and BCP were found between H(2) and the iron. On the other hand, H(2) displays four symmetrical short contacts with hydrogen atoms H(4), H(5), H(11), and H(12) from the Cp rings which encapsulate the iron, for which bond paths and BCPs were found. None of the interactions present a negative $H(r_{BCP})$ value, and therefore they can rather be considered as interactions resulting from intermolecular electrostatics. A good example is the C(6)···O(2) bond path, which appears between the closest atoms of two neighboring $2_{1[010]}$ screw

Table 7. List of BCPs Found for Selected Intermolecular Interactions

(a) **1**	R1 [Å]	R2 [Å]	R1+R2 [Å]	$\rho(r_{BCP})$ [e Å^{-3}]	$\nabla^2\rho(r_{BCP})$ [e Å^{-5}]	$G(r_{BCP})$ [Ha a_0^{-3}]	$V(r_{BCP})$ [Ha a_0^{-3}]	$H(r_{BCP})$ [Ha a_0^{-3}]
H(12B) H(6B)	1.293	1.304	2.597	0.051	0.476	0.004	−0.003	0.001
H(6C) H(12A)	1.364	1.365	2.729	0.043	0.425	0.004	−0.003	0.001
H(10) C(5)	1.220	1.652	2.872	0.061	0.618	0.005	−0.004	0.001
H(6B) C(7)	1.251	1.637	2.888	0.040	0.480	0.004	−0.003	0.001
H(2) C(9)	1.258	1.632	2.890	0.047	0.509	0.004	−0.003	0.001
(b) **2**	R1 [Å]	R2 [Å]	R1+R2 [Å]	$\rho(r_{BCP})$ [e Å^{-3}]	$\nabla^2\rho(r_{BCP})$ [e Å^{-5}]	$G(r_{BCP})$ [Ha a_0^{-3}]	$V(r_{BCP})$ [Ha a_0^{-3}]	$H(r_{BCP})$ [Ha a_0^{-3}]
H(4A) H(6C)	1.211	1.222	2.433	0.037	0.465	0.004	−0.003	0.001
H(4B) H(6C)	1.211	1.240	2.451	0.038	0.474	0.004	−0.003	0.001
H(5C) H(5C)	1.245	1.245	2.490	0.040	0.443	0.004	−0.003	0.001
H(4B) C(3)	1.277	1.709	2.986	0.042	0.465	0.004	−0.003	0.001
(c) **3**	R1 [Å]	R2 [Å]	R1+R2 [Å]	$\rho(r_{BCP})$ [e Å^{-3}]	$\nabla^2\rho(r_{BCP})$ [e Å^{-5}]	$G(r_{BCP})$ [Ha a_0^{-3}]	$V(r_{BCP})$ [Ha a_0^{-3}]	$H(r_{BCP})$ [Ha a_0^{-3}]
H(9) C(2)	1.300	1.677	2.977	0.053	0.482	0.004	−0.003	0.001
H(4) C(4)	1.327	1.821	3.148	0.030	0.386	0.003	−0.002	0.001
H(5) C(5)	1.475	1.656	3.131	0.041	0.462	0.004	−0.003	0.001
O(1) H(10)	1.494	1.011	2.505	0.054	0.578	0.005	−0.004	0.001
O(1) H(5)	1.523	1.097	2.620	0.039	0.543	0.004	−0.003	0.001
O(1) H(11)	1.554	1.081	2.635	0.040	0.451	0.004	−0.003	0.001
O(1) H(14A)	1.597	1.253	2.850	0.028	0.416	0.003	−0.002	0.001
O(1) H(7B)	1.626	1.317	2.943	0.027	0.343	0.003	−0.002	0.001
O(2) H(12)	1.455	0.972	2.427	0.059	0.733	0.006	−0.005	0.001
O(2) H(3)	1.552	0.971	2.523	0.041	0.618	0.005	−0.003	0.002
O(2) H(7A)	1.517	1.189	2.706	0.040	0.545	0.004	−0.003	0.001
O(2) H(14B)	1.607	1.101	2.708	0.028	0.423	0.003	−0.002	0.001
O(2) H(14C)	1.650	1.188	2.838	0.024	0.338	0.003	−0.002	0.001
C(6) O(2)	1.580	1.597	3.177	0.041	0.521	0.004	−0.003	0.001

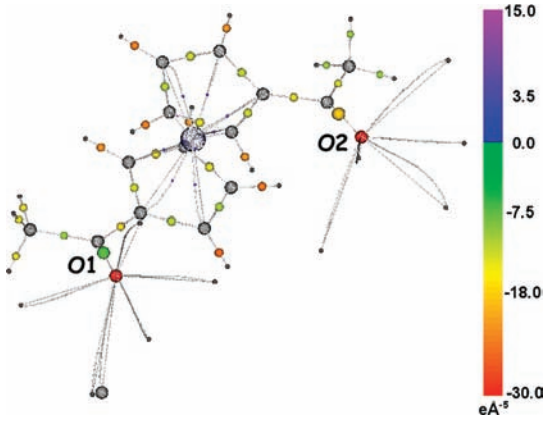

Figure 8. Map of intermolecular and C−H···O and C···O bond paths in **3** structure. The bond paths are presented as gray lines, and the BCPs are represented as spheres. The diameter of the sphere is scaled by $\rho(r_{BCP})$, while color denotes the value of $\nabla^2\rho(r_{BCP})$ (violet, positive; green to red, negative; scale from −30.0 to +15.0 e A^{-5}). [28].

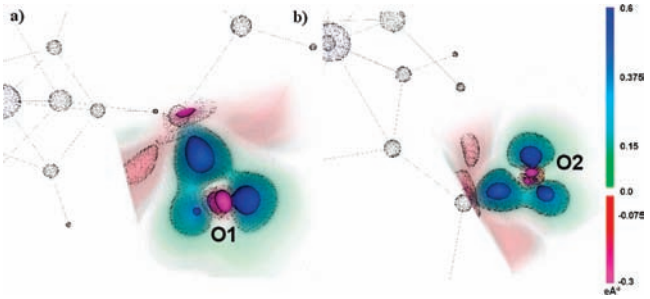

Figure 9. Visualization of the deformation density maps around the oxygen atoms (a) O(1) and (b) O(2). Solid isosurfaces at +0.6 blue and −0.3 e/A^3, transparent at +0.25 and −0.15.[28]

axis related, antiparallel oriented carbonyl groups, which may be interpreted as a set of antiparallel dipoles.

Oxygen Atom Environment in 3. Both oxygen atoms in carbonyl groups display two well separated lone electron pairs, indicated by the Lap (3, −3) (Supporting Information, Table 3S) and visible on deformation density maps, located nearly in the plane of the substituent group. However, the different environments of the two oxygen atoms are reflected in the values and distributions of the densities. In the case of O(1), the symmetrical location of the interacting hydrogen atoms H(5) and H(11) above and below the plane of the carbonyl group is reflected in a more diffused electron pair directed in between them (Figures 8 and 9a). In the case of O(2), where the most important C−H···O short contacts are in general coplanar with the acetyl group, the lone pairs are more symmetrical and condensed (Figure 9b)

Conclusions

The characterization of methyl and carbonyl groups as EDG or EWG moieties, respectively, is justified in light of the current study. The oxygen atoms acquire decidedly negative charge, while the associated carbonyl carbon atom is positively charged. Such charge distribution is in agreement with the observation that carbon atom in the carbonyl group is the target of nucleophilic attack in numerous chemical reactions. The methyl groups as a whole tend to acquire positive charge, and aromatic rings substituted by methyl moieties accumulate more negative charge than the acetyl-substituted ones.

The metal−ligand interactions in the case of all analyzed compounds present many similarities. They are characterized by relatively high charge density concentrations at BCPs, and positive laplacians as well as negative total energy densities at BCPs and the $|V(r_{BCP})|/G(r_{BCP})$ ratio in the range of 1.1−1.3. All these features are indicative of the intermediate interaction type between the ionic and covalent type, with significant degree of covalency. The monopole population of iron in all cases tend to be slightly negative, suggesting charge donation from Cp ligands. The distribution of charge over the d orbitals of metal ion illustrates a split into three groups obeying a_{1g}, e_{2g}, and e_{1g} symmetry. The percentages of total valence populations assigned to d orbitals are in good agreement with theoretical calculations. The exact differences in d-orbital populations depend on the structure of the compound.

Neither the monopole charge on the Fe atom nor the charge concentrated on Cp rings correlates with the formal oxidation potential in the analyzed compounds. Charges derived from compound **2** locate it between the compound **1** and the compound **3**. Therefore, the compound **2** in the currently studied structure is more similar to an unsubstituted ferrocene. The electron donating property of the methyl group appears to be highly directional, at least in the crystal, and compound **2** clearly illustrates the counterbalancing of such effect on the case where a whole aromatic ring is evenly substituted.

The non-intuitive low energy of the eclipsed conformation of **1** compound find some explanation in the existence of bond paths and BCPs between H atoms of the two methyls in the structure. This "H−H bonding" may stabilize the proximity of the methyl groups. Other means of stabilization seem to be electrostatic *and van der Waals* interactions of the whole molecules in the crystal lattice.

An asymmetry of the atomic surroundings of the two oxygen atoms in the **3** structure, already manifested in molecular geometry, is reflected by the differences in charge $\rho(r_{BCP})$ and $\nabla^2\rho(r_{BCP})$ values and the shape of deformation density in the regions of oxygen atoms' lone electron pairs. For all C−H···O short contacts identified by geometry criteria, bond paths and BCPs were found. However, none of the interactions proved bonding in terms total energy density.

Acknowledgment. X-ray single crystal measurements were accomplished at the Structural Research Lab. of the Chemistry Department, Warsaw University, Poland, established with a financial support from European Regional Development Found in the Sectoral Operational Programme "Improvement of the Competitiveness of Enterprises, years 2004−2006" project no. WKP_ 1/1.4.3./1/2004/72/72/165/2005/U. A.M.M. thanks for financial support within the Polish Ministry of Science and Higher Education grant for PhD students number N N204 0302 33, and additional support of the Foundation for the Polish Science-2008 grant for young researchers. K.W. thanks for a financial support from the Ministry of Science and Higher Education - Grant 1 T09A 116 30. Support

(55) Borissova, A. O.; Antipin, M. Y.; Perekalin, D. S.; Lyssenko, K. A. *CrystEngComm* **2008**, *10*, 827–832.

from the Foundation for Polish Science for K.W. and A.M.M. (Mistrz professorship) is greatly acknowledged.

Supporting Information Available: The fractal dimension plots generated for 3D residual density maps, the normal probability plots generated against full data sets for final multipole models, full lists of C−H BCPs found, a list of $-\nabla^2\rho(r_{BCP})$ critical points, indicating charge concentrations (signature 3, −3), saddle points (3, −1), and ring critical points (3, +1), a table containing numerical values of the integrated properties analyzed in this work and full lists of intermolecular BCPs found for compound **1**−**3**. This material is available free of charge via the Internet at http://pubs.acs.org. Structural data and the final multipole models for the compounds **1**, **2**, and **3** have been deposited at CSD and are available on request: compound **1** structure CSD 759982, multipole model CSD 759983, compound **2** structure CSD 759984, multipole model CSD 759985, compound **3** structure CSD 759986, multipole model CSD 759987.